Energy Storage Materials 34 (2021) 203–210

Contents lists available at ScienceDirect

Energy Storage Materials

journal homepage: www.elsevier.com/locate/ensm

Stable aqueous Zn–Ag and Zn–polyoxometalate hybrid battery driven by successive Ag^+ cation and polyoxoanion redox reactions

Kai Yang[a], Yuxuan Ying[a], Lulu Cui[a], Jianchao Sun[b], Hao Luo[c], Yuanyuan Hu[a,*], Junwei Zhao[a,*]

[a] Henan Key Laboratory of Polyoxometalate Chemistry, College of Chemistry and Chemical Engineering, Henan University, Kaifeng, Henan 475004, China
[b] School of Environment and Materials Engineering, Yantai University, Yantai, Shandong 264005, China
[c] MIIT Key Laboratory of Critical Materials Technology for New Energy Conversion and Storage, School of Chemistry and Chemical Engineering, Harbin Institute of Technology, Harbin 150001, China

ARTICLE INFO

Keywords:
Polyoxometalate
Cathode material
Energy storage mechanism
Aqueous zinc-based battery
Hybrid battery

ABSTRACT

Hybrid batteries with multiple electrochemical reactions that integrate respective advantages and remedy intricate shortages of disparate batteries are both fundamentally interesting and practically attractive. Here, an aqueous hybrid battery combining electrochemical features of Zn–Ag battery and Zn–POM battery is for the first time proposed, which is actuated by successive Ag^+ cation and polyoxoanion redox reactions in an insoluble polyoxometalate (POM)-based cathode. The unique POM-based composite material constructed from loose stacking high-nuclearity polyoxovanadate clusters and crystalline Ag nanoparticles not only provides plentiful Zn^{2+} storage sites but also presents fast ion / electron diffusion kinetics. Meanwhile, both the severe migration of Ag^+ ions and the dissolution of POM clusters in aqueous electrolyte are effectively inhibited. The as-fabricated hybrid battery with POM-based cathode exhibits a reversible capacity of 200 mAh g^{-1} at 10 A g^{-1} with outstanding capacity retention (97.4% over 7000 cycles) and superior rate capability. Moreover, the stable hybrid energy storage mechanism is revealed in detail. The work presents a promising strategy for the application of POM-based electrode in aqueous batteries and provides heuristic thinking for further developing novel energy storage systems.

1. Introduction

Designing and developing advanced batteries with long cycle life, high energy and power densities, safety reliability and affordable cost has been a focus of global concern to meet people's energy needs in electronics, electric vehicles and smart grids [1,2]. Besides widespread commercially applied lithium ion batteries, very promising aqueous Zn-based batteries (e.g. Zn–ion battery (ZIB), Zn–Ag battery (ZAB), Zn–Ni battery and Zn–air battery) have aroused increasing attention due to their inherent merits of cost-effectivity, nonflammability and environmental benignity [3–7]. As one of the most mature Zn-based batteries with high operating voltage (>1 V), theoretical energy density (600 Wh kg^{-1}) and power density (2500 W kg^{-1}), ZABs equipped with Ag or silver oxide-based cathodes have already been studied [3,4]. However, the migration of silver ions can lead to metal Ag dendrite growth inside the separator and counter electrode poisoning, resulting in poor cycle performance, which is the main obstacle for enhancing the long-life cycle in rechargeable ZABs [3,8,9]. In recent years, some tentative attempts have been made to alleviate the Ag^+ migration by optimizing electrolytes and separators to restrain the dissolution and diffusion of Ag^+ ions, nevertheless, the relevant progress is underdeveloped [9,10]. As a result, persistently seeking and finding simple and effective strategies to realize a stable ZAB system with the long-life cycle is still a severe challenge.

Very recently, aqueous ZIBs are emerging as the most compelling candidates on account of high capacity and mild electrochemical reaction environments with neutral (or slightly acidic) electrolytes [11–15]. Various crystalline Zn^{2+} host materials such as MnO_2 [16,17], V_2O_5 [18–20], $KCuFe(CN)_6$ [21], etc. have been developed [12,22–24]. It has proved that crystalline materials with large particle sizes restrict ion diffusion due to the close stacking lattices generating narrow Zn^{2+} migration channels [25,26]. In contrast, amorphous metal oxides have displayed prominent advantages in energy storage areas because their loose structures equipped with ample active sites, free volume and ion channels for charge storage and diffusion [26–28]. Thus, some investigations on amorphous Zn^{2+} host materials such as $VN_{0.9}O_{15}$ [25], MnO_2 [28], V_2O_5 [29] and $FeVO_4$ [30] have been conducted, which demonstrate apparent performance improvement. The further development of novel amorphous host materials is an attractive and challenging topic. To our knowledge, there is no report on amorphous POMs that have

* Corresponding authors.
E-mail addresses: yyhu@henu.edu.cn (Y. Hu), zhaojunwei@henu.edu.cn (J. Zhao).

https://doi.org/10.1016/j.ensm.2020.09.011
Received 25 July 2020; Received in revised form 17 September 2020; Accepted 17 September 2020
Available online 21 September 2020

been applied to aqueous ZIBs so far although some crystalline POMs with flexible molecular / electronic structures and unique multi-electron redox behaviors have revealed great potential in various batteries [31–34]. Besides, the dissolution of POM species in aqueous electrolyte leads to severe capacity fading and hinder their direct applications in aqueous batteries [35]. Therefore, designing and manufacturing amorphous POM-based materials with poor solubility would provide a new opportunity for exploiting high-performance Zn^{2+} host materials and expanding the application domains of POMs.

In order to tackle the existing problems in both ZABs and POM-based ZIBs, preparing amorphous POM-based Zn^{2+} storage host with good Ag^+ and POM confinement effect is necessary and innovative. Herein, a water-soluble high-nuclearity mixed-valence POM $K_{10}[V^{IV}_{16}V^{V}_{18}O_{82}]\bullet 20H_2O$ (KV_{34}) that has demonstrated reversible multi-electron redox activity and fast Zn^{2+} diffusion kinetics [35], was utilized to prepare amorphous $Ag_x[V_{34}O_{82}]$ ($0 < x \leq 10$) (AgV_{34}) precipitates. Due to the strong electrostatic interaction between Ag^+ cations and polyoxoanions, there is no enough time to orderly arrange clusters in the precipitation process, and then amorphous AgV_{34} precipitates would be produced. Meanwhile, the mixed-valence $[V^{IV}_{16}V^{V}_{18}O_{82}]^{10-}$ can efficiently reduce excess Ag^+ to Ag nanoparticles, forming an electron conductive Ag and Ag-POM composite material. During the precipitation process, the reduction reaction of Ag^+ occurs, which avails to further enhance the electron conductivity of the POM-based cathode. Using Ag@AgV_{34} as the cathode coupling with a metal Zn anode in 2.5 M $Zn(CF_3SO_3)$ aqueous electrolyte, an entirely new-type Zn-based hybrid battery that integrates the Zn–POM system with chemical valence changes of V_{34} clusters and the Zn–Ag system bearing the redox reaction of the Ag^0/Ag^+ pair has been developed (Fig. 1a), which is completely different from other reported Zn-based hybrid batteries [1,3,36–44]. Owing to the positive synergistic effect between Zn–Ag and Zn–POM systems, the hybrid battery manifests enhanced reversible capacity with admirable capacity retention, superior rate performance and long-term cycling stability.

2. Results and discussion

Crystalline KV_{34} precursor with ellipsoid-shaped $[V^{IV}_{16}V^{V}_{18}O_{82}]^{10-}$ anion with sizes of 1.27×1.58 nm^2 (Fig. 1b) was synthesized according to the reported method and shows good solubility in aqueous solution (see details in the Supplementary Material) [35,45]. The reaction of KV_{34} with $AgNO_3$ led to the formation of the insoluble Ag@AgV_{34} composite through strong electrostatic interaction between Ag^+ ions and V_{34} anions and their high redox activity (Fig. S1). Electrospray ionization mass spectrometry (ESI–MS) measurements can verify the structural integrity of the V_{34} clusters in the Ag@AgV_{34} composite (Fig. S2, Table S1). Scanning electron microscopy (SEM) and transmission electron microscopy (TEM) images (Fig. 1c-d) depict the nanosized rod-like morphologies of the as-prepared Ag@AgV_{34} composite, in which existing elements are further confirmed by EDS result (Inset in Fig. 1c). It should be noted that the selected area electron diffraction (SAED) image reveals the low crystallinity of Ag@AgV_{34} composite according to the weak diffraction rings except that the diffraction spots of (2 0 0) and (2 2 0) are assigned to crystalline Ag (JCPDS card no. 05-3759) (Inset in Fig. 1d). Scrupulously, crystallinity information was further investigated by high-resolution transmission electron microscopy (HRTEM), which validates the structure of crystalline Ag nanoparticles and amorphous AgV_{34} clusters as well (Fig. 1e-f). Specifically, the measured lattice spacing of 0.237 nm in the HRTEM image agrees well with the ordered Ag atoms in the (1 1 1) face (Fig. 1e). No well-defined lattice fringes were observed for the AgV_{34} region (Fig. 1f), revealing a very poor polycrystalline nature, which was also confirmed by X-ray diffraction (XRD) pattern. As presented in Fig. 1g, the XRD pattern of crystalline KV_{34} matches well with the simulated XRD result (CCDC no. 1671647). (1 1 1), (2 0 0) and (2 2 0) diffraction peaks of the Ag@AgV_{34} composite are well indexed with the standard peaks (Ag, JCPDS card no.

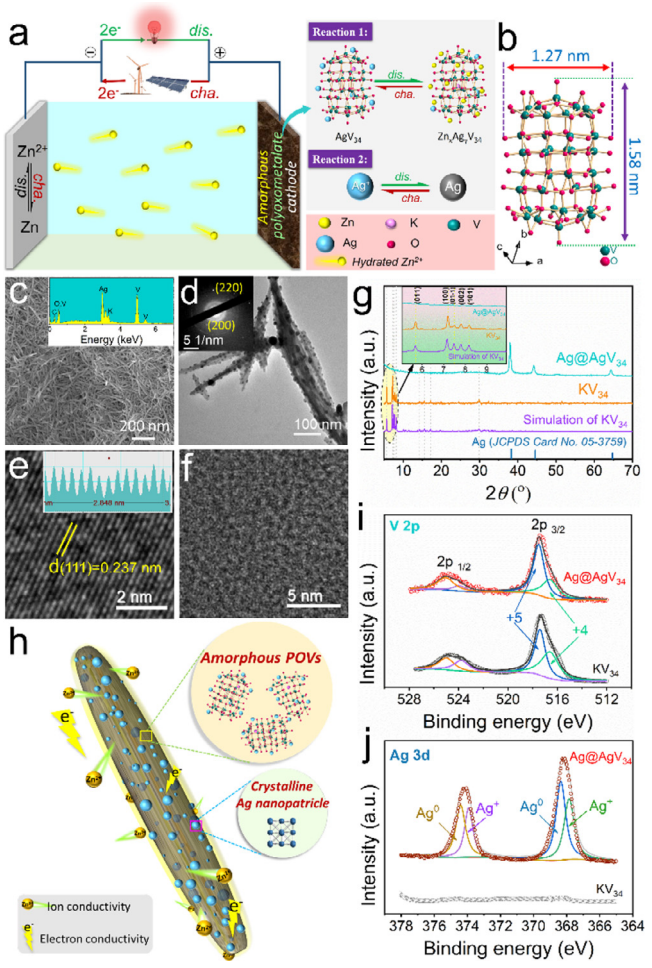

Fig. 1. (a) Schematic illustration of the rechargeable aqueous Zn–Ag and Zn–POM hybrid battery. (b) The molecular structure of the $[V^{IV}_{16}V^{V}_{18}O_{82}]^{10-}$ polyoxoanion. (c) SEM image of Ag@AgV_{34} composite material (the insert is the corresponding EDS result). (d) TEM morphology of Ag@AgV_{34} material (the insert is the corresponding SAED image). (e–f) HRTEM images for the Ag nanosphere region and AgV_{34} region in the rode–like Ag@AgV_{34} material. (g) XRD patterns of the KV_{34} and Ag@AgV_{34} materials. (h) Schematic illustration of the as-prepared composite material with fast ion and electron transport kinetics. (i–j) Comparisons of XPS spectra for V and Ag elements from the KV_{34} and Ag@AgV_{34} materials.

05-3759), in which the disappearance of other peaks indicates the random arrangement of V_{34} cluster anions *via* the rapid coprecipitation. Moreover, by virtue of high conductive Ag nanoparticles, the electrical conductivity of Ag@AgV_{34} of 7.04×10^{-4} S cm^{-1} measured at the pressure of 2 MPa via micro-four-point probe technique at ambient temperature is apparently higher than that of KV_{34} (2.41×10^{-5} S cm^{-1}). Based on above investigations, the nanosized Ag@AgV_{34} material is demonstrably identified as the composite of amorphous AgV_{34} clusters and crystalline Ag nanoparticles, which possesses fast ion and electron transport capability attributed to the uniform distribution of loose stacking AgV_{34} clusters and high conductive Ag nanoparticles (Fig. 1h). To further examine chemical valence changes of V_{34} clusters during coprecipitation process, X-ray photoelectron spectroscopy (XPS) was conducted. According to the peak areas of V^{5+} and V^{4+} (Fig. 1i), the average valence of vanadiums in V_{34} clusters increases from $V^{4.53+}$ to $V^{4.72+}$ after coprecipitation process owing to the occurrence of the redox reaction between V_{34} clusters and Ag^+ cations. Hence, it is reasonable to calculate that the molar ratio of Ag and AgV_{34} in the Ag@AgV_{34} composite should be 6.46 $mol_{(Ag)}$ / $mol_{(AgV34)}$. The facile coprecipitation method

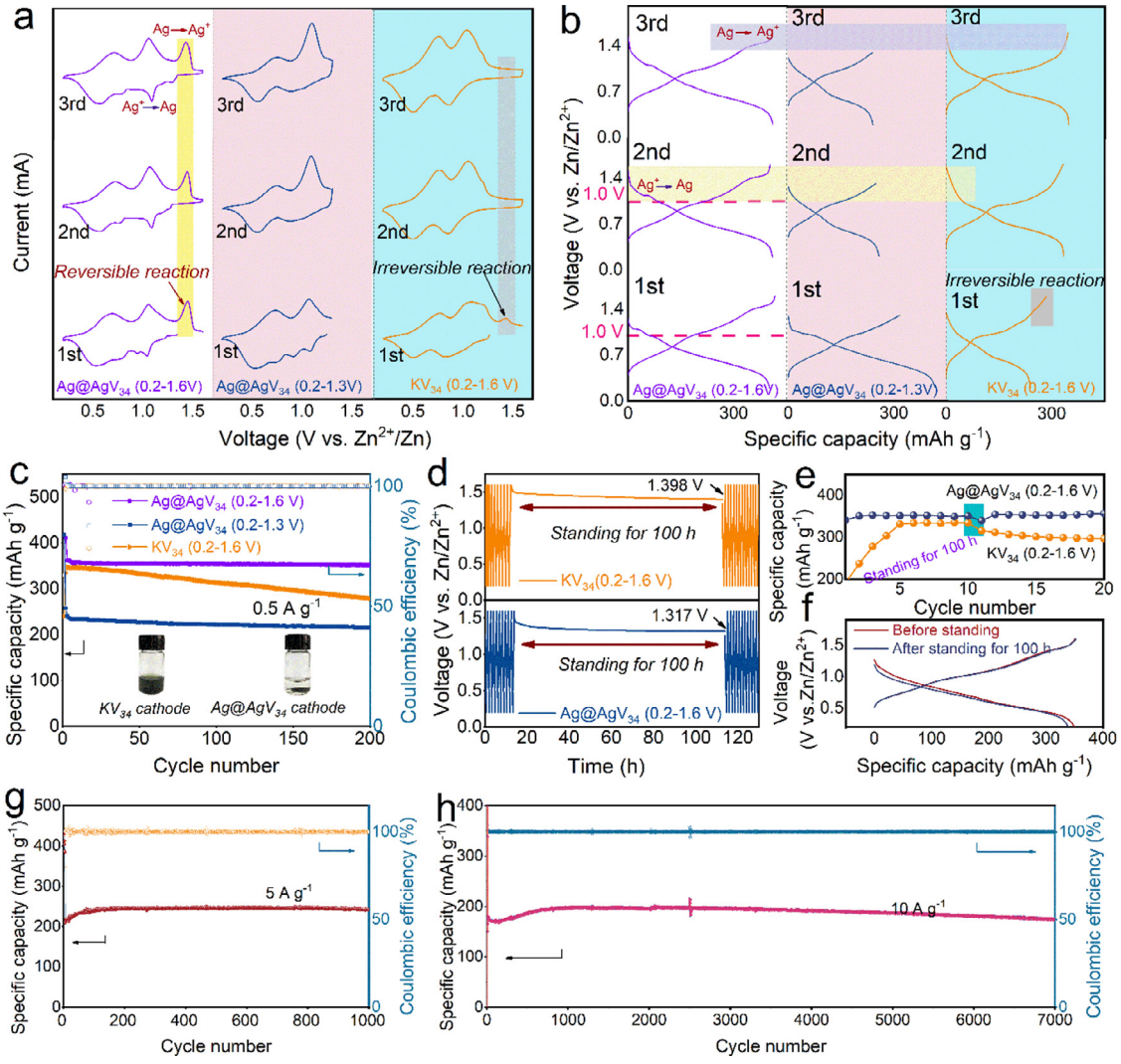

Fig. 2. (a) CV curves and (b) GCD profiles of batteries with Ag@AgV_{34} cathodes at different cut-off voltages and KV_{34} cathode at 0.2–1.6 V for the first three cycles, respectively. (c) Cycle performances of batteries with Ag@AgV_{34} cathodes at different cut-off voltages and KV_{34} cathode at a current density of 0.5 A g^{-1} (Inserts are optical images of solubility test of different cathodes in 2.5 M $Zn(CF_3SO_3)$ aqueous solutions. (d–f) Calendar life evaluation of the hybrid battery with Ag@AgV_{34} cathode and ZIB with KV_{34} cathode at a current density of 0.5 A g^{-1}: (d) Time–voltage curve of the interruption process (after the 10th charged process, the test was standing for 100 h; (e) Comparison for specific capacities of different batteries during cycling; (f) Comparison for discharge-charge profiles of hybrid battery with Ag@AgV_{34} cathode at 10th cycle (before standing) and 11th cycle (after standing for 100 h). (g, h) Cycle performances of hybrid batteries at the current densities of 5 A g^{-1} and 10 A g^{-1} at the cut-off voltage of 0.2–1.6 V.

can effectively synthesize amorphous AgV_{34} clusters with poor solubility and high oxidation state, which is beneficial to improve electrolyte permeation and reduce the solution loss of active materials in cathode. The stoichiometric ratio of Ag : K : V in AgV_{34} is 5.21 : 0.79 : 34 by inductively coupled plasma atom emission spectroscopy (ICP–AES) (Table S2). Hence, on the basis of the calculated XPS and ICP–AES results, the chemical formula of the obtained AgV_{34} cluster can be determined as $Ag_{5.21}K_{0.79}[V^{IV}_{11.80}V^{V}_{22.20}O_{82}]$. To simplify the preparation process for the mixture of Ag@AgV_{34} and conductive carbon, we further optimize the coprecipitation method to disperse conductive carbon and active material uniformly (see details in Supplementary Material). SEM and TEM images (Fig. S3) clearly elucidate the uniform distribution features of conductive additive (super P), metallic Ag nanoparticles and AgV_{34} clusters. The insoluble Ag@AgV_{34} composite consisting of amorphous AgV_{34} clusters, high conductive Ag and carbon nanoparticles provides a reliable guarantee for stable electrochemical performances.

The electrochemical performances of the cathode Ag@AgV_{34} material were conducted in CR2025-type cells with Zn foil anode, 2.5 M $Zn(CF_3SO_3)_2$ aqueous electrolyte and cellulose separator. As mentioned in our previous work, the KV_{34} cathode can generate irreversible oxidative product ($K_2V_6O_{16}$•$1.5H_2O$) in the charging voltage range of 1.4–1.5 V in the first cycle (Fig. 2a-b), which possesses inferior Zn^{2+} storage capability and thus decreases the specific capacity of Zn / KV_{34} battery [35]. While most of K^+ cations were replaced by Ag^+ cations, the irreversible reaction is substituted by the reversible Ag → Ag^+ reaction, meaning that K^+ ions are the main incentive to induce reconstruction of V–O polyhedra and then form a new crystalline phase ($K_2V_6O_{16}$•$1.5H_2O$). The marked conversion can be observed from the cyclic voltammetry (CV) curves of the Ag@AgV_{34} cathode in the cut-off voltage range of 0.2–1.6 V that the distinct oxidation peaks of the Ag@AgV_{34} cathode in the voltage range of 1.4–1.5 V still exist with similar current densities in the first three cycles, manifesting the disappearance of irreversible reaction (Fig. 2a, the faint yellow shaded area) in contrast to the oxidation peak of KV_{34} (Fig. 2a, the grayish shaded area). While the cut-off voltage range was controlled in 0.2–1.3 V, the disappearance of reduction peak after the first discharge process further affirms that the oxidation peak in 1.4–1.5 V belongs to the reversible Ag→Ag^+ reaction. Furthermore, the corresponding galvanos-

tatic charge–discharge (GCD) curves for the first three cycles also exhibit the obvious change from irreversible $KV_{34} \rightarrow K_2V_6O_{16}\bullet 1.5H_2O$ reaction to reversible $Ag \leftrightarrow Ag^+$ reaction in 1.4–1.5 V during charging process (Fig. 2b). Hence, it can be concluded that there are two relatively independent redox reactions in the Zn/Ag@AgV_{34} system in the cut-off voltage range of 0.2–1.6 V, which are the $Ag \leftrightarrow Ag^+$ reaction and $V^{5+} \leftrightarrow V^{3+}$ reaction in V_{34}, indicating that this is a hybrid system of Zn−Ag and Zn−POM batteries. Obviously, in CV curves of the Ag@AgV_{34} cathode in 0.2–1.6 V, the voltages of Ag^0/Ag^+ redox pair (1.43 / 1.10 V) are higher than those of two pairs redox peaks of V^{5+} / V^{4+} (1.06 / 0.85 V) and V^{4+} / V^{3+} (0.77 / 0.50 V), meaning that operating voltage of this hybrid battery system is enhanced. Comparison of the discharge–charge profiles of both cathodes in the first three cycles is depicted in Fig. 2b. Unlike the Zn / Ag@AgV_{34} battery with a cut-off voltage range of 0.2–1.3 V, when the cut-off voltage range of Zn / Ag@AgV_{34} battery was controlled in 0.2–1.6 V, a stable discharge platform above 1 V delivers ~20% of the total discharge specific capacity, indicative of the really enhanced operating voltage and increased specific capacity.Besides, it should be noted that there is an obvious discrepancy of the specific capacity changes between Ag@AgV_{34} and KV_{34} cathodes during the first few cycles. Upon the first cycle, the hybrid battery with Ag@AgV_{34} delivers a high capacity of 410 mAh g^{-1} at a current density of 0.05 A g^{-1} (Fig. 2b and e), suggesting that the Ag@AgV_{34} cathode provides plentiful active sites in the initial cycle [25], which is better than the crystalline KV_{34} and other reported crystalline materials (e.g. V_2O_5 [18] and MnO_2 [46,47]). In Fig. 2c, the hybrid battery with insoluble Ag@AgV_{34} yields a high reversible capacity of 362 mAh g^{-1} at a low current density of 0.5 A g^{-1} and behaves as an excellent capacity retention of 99.0% over 200 cycles in comparison with the Zn / KV_{34} battery (79.9%) in the same electrolyte dosage (see details in the Supplementary Material). Moreover, the Zn / Ag@AgV_{34} battery in the cut-off voltage range of 0.2–1.3 V still maintains a superior capacity retention, which verifies the tremendous advantage of insoluble Ag@AgV_{34} cathode in blocking Ag^+ cations and V_{34} clusters. The visible solubility test for Ag@AgV_{34} and KV_{34} cathodes for Ag@AgV_{34} and KV_{34} cathodes in electrolyte provides a more comprehensive evidence for the excellent cycle performance of Zn / Ag@AgV_{34} hybrid battery (inserts of Fig. 2c). To further evaluate their calendar life in practice, both Zn / Ag@AgV_{34} hybrid battery and Zn / KV_{34} battery that were stood for 100 h after the 10^{th} charged process show obvious voltage drop at the initial stage and then tend to be stable during the following time (Fig. 2d). The higher drop of the voltage of the Ag@AgV_{34} electrode might result from the spontaneous reduction of Ag^+ in the high oxidation state of the cathode during the long-term shelving. While restarting the cycles upon 100 h interruption, although there is slight capacity decrease in 11^{th} discharge process, the capacity is rapidly recovered in the following cycles in the Zn / Ag@AgV_{34} hybrid battery (Fig. 2e-f). But, the interrupted Zn / KV_{34} battery exhibits obvious capacity loss and rapid capacity decay during the following cycles. Comparison of the above results manifests that the Zn / Ag@AgV_{34} hybrid battery exhibits the adequate active material confinement and a good calendar life. Additionally, the high loading cathodes (2.2–9.0 mg cm^{-2}) at a current density of 0.5 A g^{-1} also exhibit acceptable cycle performance, meaning a feasibility of practical application (Fig. S4). We further investigate the cycle stability and long-term cycle life at high current densities of 5 and 10 A g^{-1} (Fig. 2g-h). The Zn / Ag@AgV_{34} hybrid battery displays a high specific capacity of 247 mAh g^{-1} with excellent cycle stability and negligible capacity decay at 5 A g^{-1} for at least 1000 cycles. Even at 10 A g^{-1}, a reversible capacity of 200 mAh g^{-1} with 97.4% capacity retention can still be achieved over 7000 cycles, which demonstrates a remarkable long cyclability, being superior to the majority of the reported results (see Table S3).

To further understand the roles of the metallic Ag and amorphous AgV_{34} for electrochemical performance improvement in the as-fabricated hybrid battery, we quantitatively analyzed the diffusion distribution and the pseudocapacitive contribution as well as the electron and Zn^{2+} diffusion kinetics in the hybrid battery with Ag@AgV_{34} cathode and ZIBs with Ag@AgV_{34} and KV_{34} cathodes by CV method, galvanostatic intermittent titration technique (GITT) and electrochemical impedance spectroscopy (EIS) measurements (Fig. 3a-b and Fig. S9). The high pseudocapacitive capacity of the KV_{34} cathode can be ascribed to the intercalation pseudocapacitive mechanism, in which Zn^{2+} ions can efficiently intercalate into the three-dimensional migration channels constructed from V_{34} nanoclusters and interact with abundant internal surface sites accompanied by a faradaic charge-transfer process [35]. The Ag@AgV_{34} cathode exhibits the strengthened capacitive-like zinc storage behavior relative to the KV_{34} cathode at various scan rates of 0.2–0.6 mV s^{-1} (Fig. 3a, Fig. S5–S7). Obviously, amorphous AgV_{34} material provides more free volume and ample active sites within the cathodes to dominate fast Zn^{2+} diffusion kinetics and effective redox reactions on the internal surface and near surface of amorphous clusters and thus increase capacitive-controlled current with a concomitant faradaic charge -transfer behavior [30,35,48–50]. Impressively, the Ag@AgV_{34} cathode with a cut-off voltage of 0.2–1.6 V reveals highest pseudocapacitive contribution at various scan rates, because the extra $Ag \leftrightarrow Ag^+$ reaction makes use of more effective Ag sites thereby boosting the capacitive-controlled contribution significantly, espically in high voltage region, which is a significant factor that realizes excellent rate performance [50]. It is evident that both Ag@AgV_{34} and KV_{34} cathodes deliver high Zn^{2+} diffusion coefficients of 10^{-8}–10^{-9} cm^2 s^{-1} during cycling, as revealed by GITT analysis, which are higher than those of reported low-nuclearity materials (10^{-9}–10^{-11} cm^2 s^{-1}) (Fig. 3b, Fig. S8) [35]. We speculate that large-volume high-nuclearity POMs play a key role in constructing sufficient ion migration channels to facilitate fast ion transport. The ion diffusion coefficient is too high to be further enhanced by stacking manner of regulating clusters. The change of diffusion coefficient is different from low-nuclearity materials, which would achieve obvious enhancement in Zn^{2+} diffusion kinetics [25,28–30]. What is noteworthy is that the random stacking clusters play a vital role in exposing more charge storage sites and the high electron conductivity of Ag nanoparticles promotes the electron transport during cycling, which are conducive to realize high rate capability [26,27,50]. Moreover, the slight Zn^{2+} diffusion coefficient enhancement of the Zn / Ag@AgV_{34} hybrid battery should be associated with the additional $Ag \leftrightarrow Ag^+$ reaction. The reversible $Ag \leftrightarrow Ag^+$ reaction process would inevitably change the phase states of the cathode thereby affect the Zn^{2+} diffusion behavior. To verify this inference, further investigations on phase changes during cycling have been carried out in the following part via *ex-situ* XRD and HRTEM measurements. Comparison of EIS results for different battery systems can favor to explain the excellent electronic conductivity and Zn^{2+} diffusion behavior (Fig. S9, Table S3). Fig. 3c compares the rate performances of the hybrid battery with the Ag@AgV_{34} cathode, the ZIB with the Ag@AgV_{34} cathode and the ZIB with the KV_{34} cathode at various current densities. As expected, the hybrid battery shows a superior rate capability in the wide cut-off voltage range (0.2–1.6 V). Comparatively, the ZIB with the Ag@AgV_{34} cathode at a cut-off voltage (0.2–1.3 V) yields a lower specific capacity at different current densities, and the ZIB with the KV_{34} cathode exhibits inferior rate performance. When cycling at current densities of 0.2, 0.5, 2, 5, 10 and 12 A g^{-1}, the as-fabricated Zn / Ag@AgV_{34} hybrid battery delivers reversible capacities of 383, 357, 305, 258, 207 and 176 mAh g^{-1}, respectively. Upon switching back to 0.2 A g^{-1}, specific capacities are recovered immediately, revealing an excellent rate performance and recovery capability. Significantly, the hybrid battery also presents a good energy density (310 Wh kg^{-1}) and an impressive power density (7.1 kW kg^{-1}) (based on the mass of active material only) (Fig. 3d), outstripping most of already reported vanadium-based hosts in aqueous ZIBs, e.g. amorphous V_2O_5 [29], $Na_{0.33}V_2O_5$ [51], $FeVO_4$ [30], VO_2(B) [52], $Li_xV_2O_5\bullet nH_2O$ [53], $VN_{0.9}O_{0.15}$ [25], $VOPO_4$ [54] and V_2O_5 [18].

The *ex-situ* XRD, XPS, ESI−MS and SEM–EDS measurements were performed to elucidate the changes of phase behavior and electrochemical reaction mechanism of Zn / Ag@AgV_{34} hybrid battery during discharge / charge processes. Fig. 4a illustrates the *ex-situ* XRD patterns of

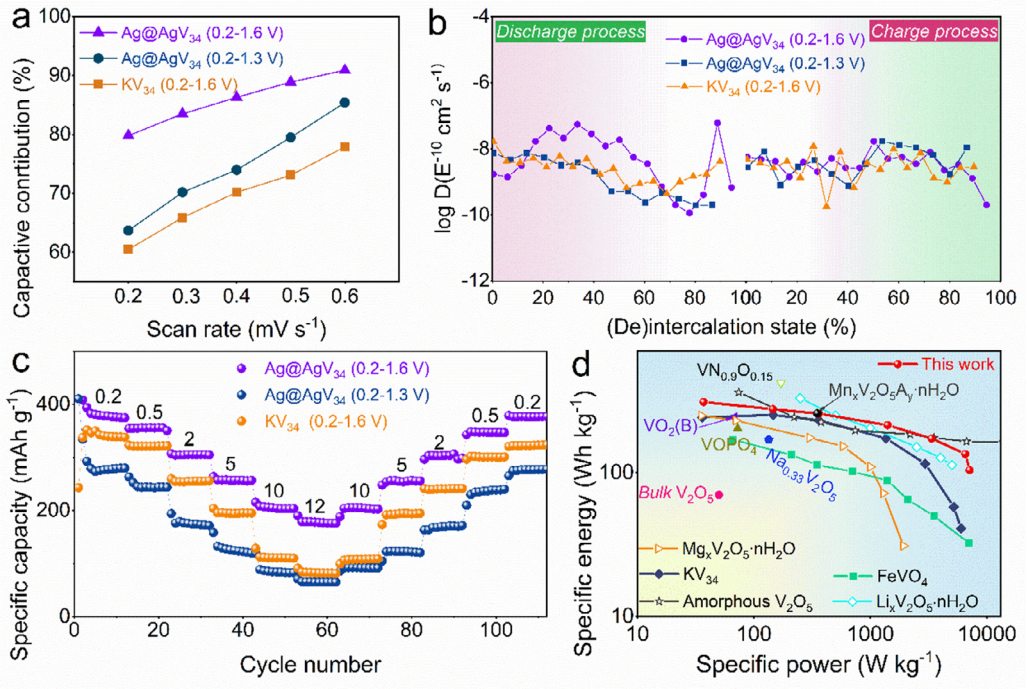

Fig. 3. (a) Comparison of pseudocapacitive contribution for $Ag@AgV_{34}$ and KV_{34} cathodes at different scan rates. (b) Diffusivity coefficients of Zn^{2+} in cathodes during the charging and discharging processes of the stable cycle. (c) Rate capability of the hybrid battery at different current densities from 0.2–12 A g^{-1}. (d) Ragone plots: comparison of energy and power densities of Zn–Ag / Zn–POM hybrid batteries with ZIBs based on other reported cathodes.

the $Ag@AgV_{34}$ cathode during the first two cycles. During the first discharging process, a new phase that is identified as the reduction product $V_{13}O_{16}$ (marked with ♠, JCPDS card no. 07–7708, Fig. S10) appears at the discharge voltage of 0.68 V and is clearly observed at the full discharged state (0.2 V), and then disappears upon charging from 0.2 to 1.35 V. The following discharge–charge processes exhibit the same evolution as the former, revealing the reversible product ($V_{13}O_{16}$) and phase conversion upon cycling. During the first charging process from 1.35 V to 1.6 V, the peak intensity of metal Ag decreases gradually, and a series of new sharp peaks marked with ♦ appear, indexing to the most possible phase of $Ag(VO_3)$ (JCPDS card no. 05–0645), which demonstrates that crystalline Ag nanoparticles from the original composite material also participate in the cathodic reaction. In subsequent discharging process, the peak intensities of the new phase gradually diminish and then disappear until discharging to 0.5 V. Upon switching to charging process, the new phase reappears and the intensity increases accompanied by the peak intensity of metal Ag decreasing regularly, indicative of the reversible formation / decomposition conversions of $Ag \leftrightarrow Ag(VO_3)$, which is conducive to explain the aforementioned slight change of Zn^{2+} diffusion behavior in the Zn / $Ag@AgV_{34}$ hybrid battery with a cut-off voltage of 0.2–1.6 V. Accordingly, our previous work has proved that the V_{34} clusters have highly reversible Zn^{2+} intercalation / deintercalation behavior and structure stability [35]. The *ex-situ* TEM has been carried out to further observe the emerging phases during cycling, in which the amorphous AgV_{34} region, reversible reduction product ($V_{13}O_{16}$) and Ag^0 at the full discharged state, as well as the amorphous AgV_{34} region and reversible oxidative product ($Ag(VO_3)$) at the full charged state can be clearly observed in SAED patterns and HRTEM images (Fig. 4b-e). The existence of V_{34} clusters at the full charged / discharged states has been also confirmed by ESI–MS measurement (Fig. S2). All of these evidences can favor to indicate that V_{34} clusters undergo reversible redox reaction and maintain amorphous phase state during cycling, which verifies the structural integrity of the V_{34} clusters in the $Ag@AgV_{34}$ composite during the charge–discgarge process. Additionally, the reaction mechanism of the hybrid battery has been further probed by insight into chemical valence states of Zn, V and Ag elements in the $Ag@AgV_{34}$ cathode via XPS analysis (Fig. 4f, Fig. S11). The effective Zn^{2+} intercalation / deintercalation behavior can be confirmed by the well-marked intensity changes of Zn 2p peaks at full discharged (0.2 V) and charged (1.6 V) states. From the high-resolution V 2p spectra, the presence of V^{5+} and V^{4+} ions has been confirmed in the initial $Ag@AgV_{34}$ cathode. After discharging to 0.2 V, the V 2p peaks shift to lower binding energy due to the reduction of V^{5+} and V^{4+} ions, which shows that V^{5+} ions vanish and V^{3+} ions are detected. Subsequently, when the cell was fully charged to 1.6 V, V^{3+} and V^{4+} ions are oxidized to high-valence vanadium ions accompaning the appearance of V^{5+} ions as well as the disappearance of V^{3+} ions, suggesting the deintercalation behavior of Zn^{2+} ions in the $Ag@AgV_{34}$ cathode. As indicated by the Ag 3d spectrum, the ratio of Ag^+ / Ag^0 decreases from 1.13 to 0.178 upon discharging to 0.2 V, indicating that the Ag^+ ions reduce to metal Ag. When recharging to 1.6 V, the vast majority of metal Ag are redoxized to Ag^+ ions with a high Ag^+ / Ag^0 ratio (5.60). These results affirm the existence of reversible redox pair of Ag^0/Ag^+ in the hybrid battery system. The morphology information of the $Ag@AgV_{34}$ cathode at the full charged and discharged states was also investigated by SEM and TEM (Fig. S12). It can be seen from the SEM images that the rod-like $Ag@AgV_{34}$ composite material would turn into flaky morphology after discharged to 0.2 V, and then further turn into linear morphology upon charging process. The morphology changes are also observed from TEM images. Although the morphology of the $Ag@AgV_{34}$ cathode has been changed, the Zn / $Ag@AgV_{34}$ battery system still exhibits stable electrochemical performance. In order to inquiry the solvation and migration behaviors of Ag^+ ions and V_{34} clusters in the hybrid battery, we further detect the Zn anode after 5^{th} and 50^{th} cycles by SEM–EDS to collect the signals of Ag and V elements (Fig. 4g, Fig. S13). Additionally, the contents of Ag and V atoms in high concentration electrolyte upon 5 cycles were also detected by ICP–AES (Table S2). The obtained SEM–EDS and ICP–AES results prove the insoluble feature of $Ag@AgV_{34}$ during discharge-charge process, owing to the effective synergistic immobilization of V_{34} clusters and Ag^+ ions in the $Ag@AgV_{34}$ cathode. According to

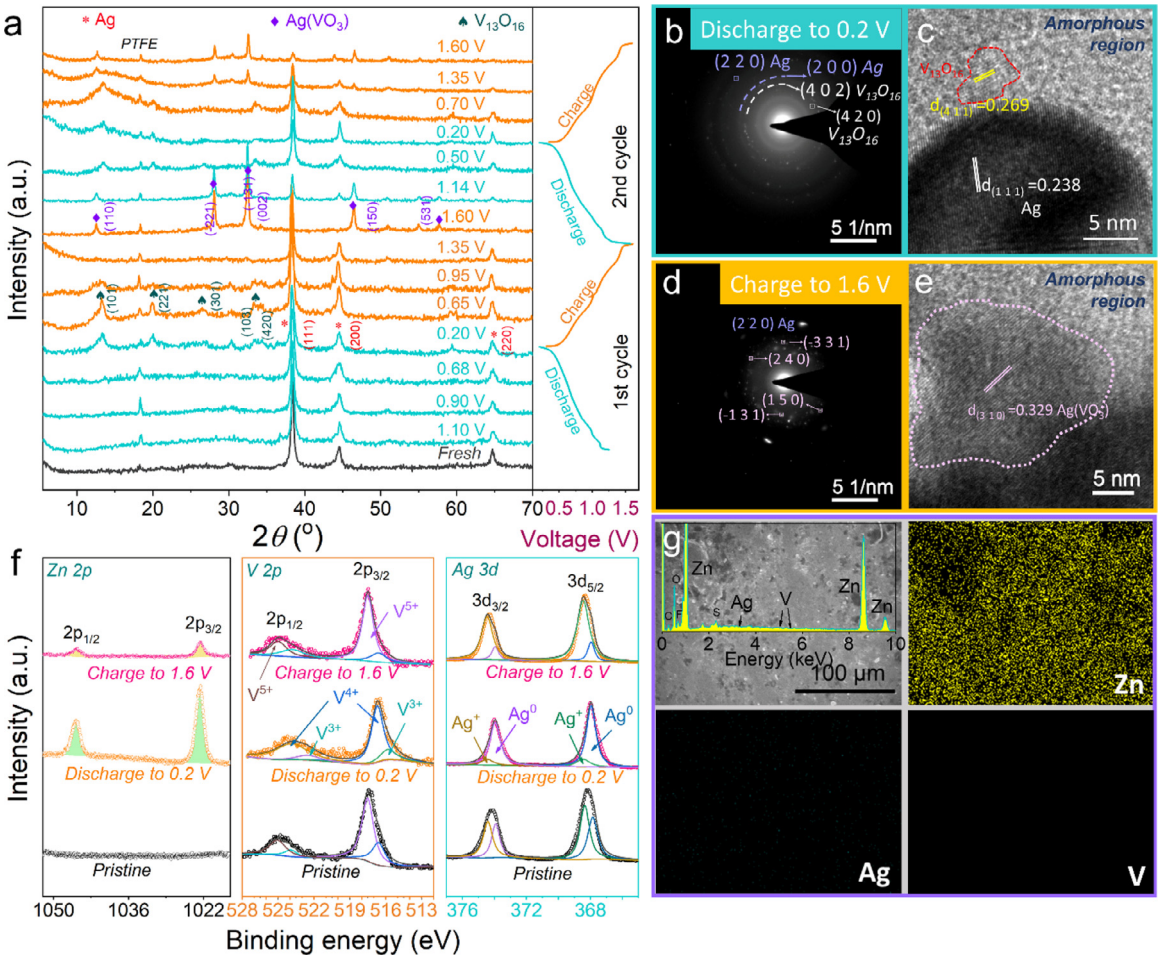

Fig. 4. (a) *Ex situ* XRD patterns of the Ag@AgV$_{34}$ cathodes at different voltages of the first two cycles. (b-e) SAED and HRTEM images of the Ag@AgV$_{34}$ cathodes at the 2nd full discharged (b-c) and charged (d-e) states. (f) High−resolution XPS spectra for Zn 2p, V 2p and Ag 3d elements at initial and 10th full charged/discharged states of Ag@AgV$_{34}$ cathodes. (g) The surface morphology of Zn anode after 5 cycles and EDS mapping results of Zn, Ag and V elements on the surface of Zn anode (The insert is the EDS curve of all elements scanning).

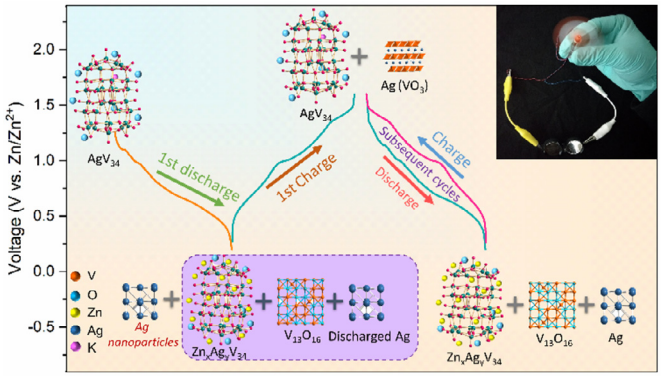

Fig. 5. Schematic illustration of redox reaction process in the Ag@AgV$_{34}$ cathode during cycling. The insert shows a photograph of two Zn/Ag@AgV$_{34}$ cells in series to power a mini motor with a fan.

the above analysis, the energy storage mechanism can be clearly summarized in Fig. 5 and the following reaction equation. In the first discharging process, Zn^{2+} ions inserted into amorphous AgV_{34} cathode trigger a series of reduction reactions to produce more metal Ag (discharged Ag), amorphous reduced V_{34} and highly- reduced $V_{13}O_{16}$. Upon switching to charging process, the inserted Zn^{2+} ions are extracted, and the reduction products $V_{13}O_{16}$ and metal Ag (including discharged Ag and crystalline Ag nanoparticles from the original Ag@AgV$_{34}$ composite) are oxidized to form fully-oxidised Ag(VO_3) upon charging, and reduced V_{34} clusters are also oxidized. During the subsequent cycles, the charged products (oxidized V_{34} clusters and Ag(VO_3)) and the discharged products (metallic Ag, reduced V_{34} clusters and $V_{13}O_{16}$) in the cathode participate in the continuous Zn^{2+} intercalation / deintercalation process synergistically, which can proceed thousands of cycles steadily in the hybrid battery system. In addition, two in-series Zn/Ag@AgV$_{34}$ hybrid batteries can power a mini motor with a fan for several hours, illustrating its great application potential in practice. In detail, the electrochemical reaction mechanism of hybrid battery is formulated as follows:

The first cycle

Discharge process:

Cathode:

$$Ag_{5.21}K_{0.79}[V_{34}O_{82}] + yZn^{2+} + 2ye^- \rightarrow Ag_{(5.21-x)}K_{0.79}Zn_y[V_{34}O_{82}]_m + 2.62(1-m)V_{13}O_{16} + xAg \quad (1)$$

$$\text{Anode}: yZn \rightarrow yZn^{2+} + 2ye^- \quad (2)$$

Charge process:

Cathode:

$$Ag_{(5.21-x)}K_{0.79}Zn_{0.5y}[V_{34}O_{82}]_m + 2.62(1-m)V_{13}O_{16} + (6.46+x)Ag \rightarrow Ag_{(11.67-n)}K_{0.79}Zn_{(0.5y-z)}[V_{34}O_{82}]_{(1-34/n)} + nAg(VO_3) + zZn^{2+} + 2ze^- \quad (3)$$

$$\text{Anode}: zZn^{2+} + 2ze^- \rightarrow zZn \quad (4)$$

The subsequently cycles:

$$\text{Cathode}: Ag_{(11.67-n)}K_{0.79}Zn_{(0.5y-z)}\left[V_{34}O_{82}\right]_{(1-34/n)} + nAg\left(VO_3\right) + zZn^{2+} + 2ze^- \leftrightarrow Ag_{(5.21-x)}K_{0.79}Zn_{0.5y}\left[V_{34}O_{82}\right]_m + 2.62(1-m)V_{13}O_{16} + (6.46+x)Ag \quad (5)$$

$$\text{Anode}: zZn \leftrightarrow zZn^{2+} + 2ze^- \quad (6)$$

Overall reaction:

$$Ag_{(11.67-n)}K_{0.79}Zn_{(0.5y-z)}\left[V_{34}O_{82}\right]_{(1-34/n)} + nAg\left(VO_3\right) + zZn \leftrightarrow Ag_{(5.21-x)}K_{0.79}Zn_{0.5y}\left[V_{34}O_{82}\right]_m + 2.62(1-m)V_{13}O_{16} + (6.46+x)Ag \quad (7)$$

In summary, the electrochemical reaction of the hybrid battery can be given the credit to the following merits: (1) the metal Ag nanoparticles loaded the amorphous AgV_{34} material can provide more free volume and charge storage sites within the cathodes to dominate fast Zn^{2+} and electron diffusion kinetics, giving rise to enhanced energy and power density; (2) the confirmed redox pair of Ag^0 / Ag^+ provides extra Zn^{2+} storage sites and boosts discharge voltage to yield a high energy density; (3) the positive synergistic confinement effect between Ag^+ cations and V_{34} clusters can inhibit the dissolution and migration of V_{34} clusters and Ag^+ cations in the $Ag@AgV_{34}$ cathode, resulting in excellent capacity retention and long cycle life; (4) the sharp decreasement of K^+ ions in the $Ag@AgV_{34}$ cathode eliminates the adverse irreversible reaction. In short, amorphous structure of the $Ag@AgV_{34}$ cathode material and the interaction of V_{34} clusters and Ag^+ cations in the $Ag@AgV_{34}$ cathode can make for solving the existing problems of Zn–Ag and Zn–POM systems and achieve the advanced hybrid battery with superior electrochemical performances.

3. Conclusion and outlook

We discovered the first aqueous hybrid battery with an amorphous POM-based composite cathode that integrates electrochemical features of Zn−Ag battery and Zn−POM battery through successive Ag^+ cationic and polyoxoanionic redox reactions. It should be noted that crystalline Ag nanoparticles and loose packing POM clusters in the matrix engineer unobstructed ion / electron diffusion kinetics. Furthermore, strong electrostatic interactions between Ag^+ cations and polyoxoanions efficiently restrain the severe solubility and diffusion behavior of Ag^+ ions and polyoxoanions, which realizes advantage-complementary of different battery systems. As expected, the $Zn/Ag@AgV_{34}$ hybrid battery yields a good rate capability, high reversible capacity with enhanced capacity retention and a long lifespan, demonstrating a prospective energy storage system with competitive energy density (310 Wh kg^{-1}) and power density (7.1 kW kg^{-1}) and revealing a stable hybrid energy storage mechanism. Our encouraging results offer broad prospects to develop reliable POM-based electrode materials for Zn-based batteries, which could also be extended to other energy storage systems.

Declaration of Competing Interest

The authors declare no competing interests.

CRediT authorship contribution statement

Kai Yang: Conceptualization, Data curation, Formal analysis, Writing - original draft, Writing - review & editing. **Yuxuan Ying:** Data curation, Investigation. **Lulu Cui:** Data curation, Investigation. **Jianchao Sun:** Conceptualization, Methodology. **Hao Luo:** Conceptualization, Methodology. **Yuanyuan Hu:** Conceptualization, Formal analysis, Funding acquisition, Writing - original draft, Writing - review & editing. **Junwei Zhao:** Conceptualization, Project administration, Resources, Supervision, Validation, Formal analysis, Funding acquisition, Writing - original draft, Writing - review & editing.

Acknowledgments

This work was financially supported by the National Natural Science Foundation of China (21871077, 21671054, 21771052, 21902044), the Program for Innovation Teams in Science and Technology in Universities of Henan Province (20IRTSTHN004), China Postdoctoral Science Foundation (2019M652517), the Major Project of Science and Technology, Education Department of Henan Province (202102310224), the Program of First-Class Discipline Cultivation Project of Henan University (2019YLZDYJ02, CJ1205A0240019) and the 2019 Students Innovative Pilot Plan of Henan University (201910475033, 201910475034).

Supplementary materials

Supplementary material associated with this article can be found, in the online version, at doi:10.1016/j.ensm.2020.09.011.

References

[1] B. Li, J. Quan, A. Loh, J. Chai, Y. Chen, C. Tan, X. Ge, T.S. Hor, Z. Liu, H. Zhang, Y. Zong, Nano Lett. 17 (2017) 156–163.
[2] C. Yang, J. Chen, X. Ji, T.P. Pollard, X. Lu, C.J. Sun, S. Hou, Q. Liu, C. Liu, T. Qing, Y. Wang, O. Borodin, Y. Ren, K. Xu, C. Wang, Nature 569 (2019) 245–250.
[3] P. Tan, B. Chen, H. Xu, W. Cai, W. He, H. Zhang, M. Liu, Z. Shao, M. Ni, ACS Appl. Mater. Interfaces 10 (2018) 36873–36881.
[4] C.-C. Chang, Y.-C. Lee, H.-J. Liao, Y.-T. Kao, J.-Y. An, D.-Y. Wang, ACS Sustain. Chem. Eng. 7 (2018) 2860–2866.
[5] Y. Li, J. Fu, C. Zhong, T. Wu, Z. Chen, W. Hu, K. Amine, J. Lu, Adv. Energy Mater. 9 (2019) 1802605.
[6] R. Kumar, K.M. Johnson, N.X. Williams, V. Subramanian, Adv. Energy Mater. 9 (2019) 1803645.
[7] B. Tang, L. Shan, S. Liang, J. Zhou, Energy Environ. Sci. 12 (2019) 3288–3304.
[8] C. Li, Q. Zhang, T. Li, Z. Zhu, B. He, Z. Zhou, P. Man, Q. Li, Y. Yao, J. Mater. Chem. A 7 (2019) 2034–2040.
[9] A.M. Zamarayeva, A.M. Gaikwad, I. Deckman, M. Wang, B. Khau, D.A. Steingart, A.C. Arias, Adv. Electron. Mater. 2 (2016) 1500296.
[10] B. Kyle, S. Vivek, Adv. Mater. 27 (2015) 689–694.
[11] Y. Zeng, Z. Lai, Y. Han, H. Zhang, S. Xie, X. Lu, Adv. Mater. 30 (2018) 1802396.
[12] G. Fang, J. Zhou, A. Pan, S. Liang, ACS Energy Lett. 3 (2018) 2480–2501.
[13] J. Huang, Z. Guo, Y. Ma, D. Bin, Y. Wang, Y. Xia, Small Methods 3 (2019) 1800272.
[14] A. Konarov, N. Voronina, J.H. Jo, Z. Bakenov, Y.-K. Sun, S.-T. Myung, ACS Energy Lett. 3 (2018) 2620–2640.
[15] H. Luo, B. Wang, F. Wang, J. Yang, F. Wu, Y. Ning, Y. Zhou, D. Wang, H. Liu, S.X. Dou, ACS Nano 14 (2020) 7328–7337.
[16] J. Huang, Z. Wang, M. Hou, X. Dong, Y. Liu, Y. Wang, Y. Xia, Nat. Commun. 9 (2018) 2906.
[17] W. Sun, F. Wang, S. Hou, C. Yang, X. Fan, Z. Ma, T. Gao, F. Han, R. Hu, M. Zhu, C. Wang, J. Am. Chem. Soc. 139 (2017) 9775–9778.
[18] J. Zhou, L. Shan, Z. Wu, X. Guo, G. Fang, S. Liang, Chem. Commun. 54 (2018) 4457–4460.
[19] P. Hu, T. Zhu, J. Ma, C. Cai, G. Hu, X. Wang, Z. Liu, L. Zhou, L. Mai, Chem. Commun. 55 (2019) 8486–8489.
[20] D. Chen, X. Rui, Q. Zhang, H. Geng, L. Gan, W. Zhang, C. Li, S. Huang, Y. Yu, Nano Energy 60 (2019) 171–178.
[21] Z. Jia, B. Wang, Y.J.M.C. Wang, Physics 149 (2015) 601–606.
[22] M. Song, H. Tan, D. Chao, H.J. Fan, Adv. Funct. Mater. 28 (2018) 1802564.
[23] F. Wan, Z. Niu, Angew. Chem. Int. Ed. 58 (2019) 2–12.
[24] S. Liu, L. Kang, J.M. Kim, Y.T. Chun, J. Zhang, S.C. Jun, Adv. Energy Mater. 10 (2020) 2000477.
[25] J. Ding, Z. Du, B. Li, L. Wang, S. Wang, Y. Gong, S. Yang, Adv. Mater. 44 (2019) 1904369.
[26] J. Liu, M. Zheng, X. Shi, H. Zeng, H. Xia, Adv. Funct. Mater. 26 (2016) 919–930.
[27] S. Yan, K. Abhilash, L. Tang, M. Yang, Y. Ma, Q. Xia, Q. Guo, H. Xia, Small 15 (2019) 1804371.
[28] Y. Wu, J. Fee, Z. Tobin, A. Shirazi-Amin, P. Kerns, S. Dissanayake, A. Mirich, S.L. Suib, ACS Appl. Energy Mater. 3 (2020) 1627–1633.
[29] X. Wang, Y. Li, S. Wang, F. Zhou, P. Das, C. Sun, S. Zheng, Z.-S. Wu, Adv. Energy Mater. 10 (2020) 2000081.
[30] Y. Luo, L. Wei, H. Geng, Y. Zhang, Y. Yang, C. Li, ACS Appl. Mater. Interfaces 12 (2020) 11753–11760.
[31] Y. Nishimoto, D. Yokogawa, H. Yoshikawa, K. Awaga, S. Irle, J. Am. Chem. Soc. 136 (2014) 9042–9052.
[32] T. Wei, M. Zhang, P. Wu, Y.-J. Tang, S.-L. Li, F.-C. Shen, X.-L. Wang, X.-P. Zhou, Y.-Q. Lan, Nano Energy 34 (2017) 205–214.
[33] J.C. Ye, J.J. Chen, R.M. Yuan, D.R. Deng, M.S. Zheng, L. Cronin, Q.F. Dong, J. Am. Chem. Soc. 140 (2018) 3134–3138.
[34] Y. Hayashi, Coord. Chem. Rev. 255 (2011) 2270–2280.
[35] K. Yang, Y. Hu, L. Li, L. Cui, L. He, S. Wang, J. Zhao, Y.-F. Song, Nano Energy 74 (2020) 104851.
[36] W. Xiong, D. Yang, T.K. Hoang, M. Ahmed, J. Zhi, X. Qiu, P. Chen, Energy Storage Mater. 15 (2018) 131–138.

[37] S. Chen, R. Lan, J. Humphreys, S. Tao, ACS Appl. Energy Mater. 3 (2020) 2526–2536.
[38] M. Huang, J. Meng, Z. Huang, X. Wang, L. Mai, J. Mater. Chem. A 8 (2020) 6631–6637.
[39] T. Wei, Q. Li, G. Yang, C. Wang, Adv. Energy Mater. 9 (2019) 1901480.
[40] Q. Zhang, Y. Lu, L. Miao, Q. Zhao, K. Xia, J. Liang, S.L. Chou, J. Chen, Angew. Chem. Int. Ed. 57 (2018) 14796–14800.
[41] S. Islam, M.H. Alfaruqi, D.Y. Putro, V. Mathew, S. Kim, J. Jo, S. Kim, Y.K. Sun, K. Kim, J. Kim, ChemSusChem 11 (2018) 2239–2247.
[42] Y.P. Deng, R. Liang, G. Jiang, Y. Jiang, A. Yu, Z. Chen, ACS Energy Lett. 5 (2020) 1665–1675.
[43] H. Li, C.J. Firby, A.Y. Elezzabi, Joule 3 (2019) 2268–2278.
[44] D. Chao, C. Ye, F. Xie, W. Zhou, Q. Zhang, Q. Gu, K. Davey, L. Gu, S.Z. Qiao, Adv. Mater. 32 (2020) e2001894.
[45] A. Müller, R. Rohlfing, J. Döring, M. Penk, Angew. Chem. Int. Ed. Engl. 30 (1991) 588–590.
[46] G. Fang, C. Zhu, M. Chen, J. Zhou, B. Tang, X. Cao, X. Zheng, A. Pan, S. Liang, Adv. Funct. Mater. 29 (2019) 1808375.
[47] L. Wang, X. Cao, L. Xu, J. Chen, J. Zheng, ACS Sustain. Chem. Eng. 6 (2018) 16055–16063.
[48] G. Fang, S. Liang, Z. Chen, P. Cui, X. Zheng, A. Pan, B. Lu, X. Lu, J. Zhou, Adv. Funct. Mater. 44 (2019) 1905267.
[49] V. Augustyn, P. Simon, B. Dunn, Energy Environ. Sci. 7 (2014) 1597–1614.
[50] Y Cai, R. Chua, S. Huang, H. Ren, M. Srinivasan, Chem. Eng. J. 396 (2020) 125221–125229.
[51] P. He, G. Zhang, X. Liao, M. Yan, X. Xu, Q. An, J. Liu, L. Mai, Adv. Energy Mater. 8 (2018) 1702463.
[52] J. Ding, Z. Du, L. Gu, B. Li, L. Wang, S. Wang, Y. Gong, S. Yang, Adv. Mater. 30 (2018) 1800762.
[53] Y. Yang, Y. Tang, G. Fang, L. Shan, J. Guo, W. Zhang, C. Wang, L. Wang, J. Zhou, S. Liang, Energy Environ. Sci. 11 (2018) 3157–3162.
[54] F. Wan, Y. Zhang, L. Zhang, D. Liu, C. Wang, L. Song, Z. Niu, J. Chen, Angew. Chem. Int. Ed. 58 (2019) 7062–7067.